JACS Au
AN OPEN ACCESS JOURNAL OF THE AMERICAN CHEMICAL SOCIETY

Photodynamic Hydrogen-Bonded Biohybrid Framework: A Photobiocatalytic Cascade Nanoreactor for Accelerating Diabetic Wound Therapy

Wei Huang,□ Haitao Yuan,□ Huangsheng Yang, Linjing Tong, Rui Gao, Xiaoxue Kou, Jigang Wang,* Xiaomin Ma, Siming Huang,* Fang Zhu, Guosheng Chen,* and Gangfeng Ouyang

Cite This: *JACS Au* 2022, 2, 2048−2058

Read Online

ACCESS | Metrics & More | Article Recommendations | Supporting Information

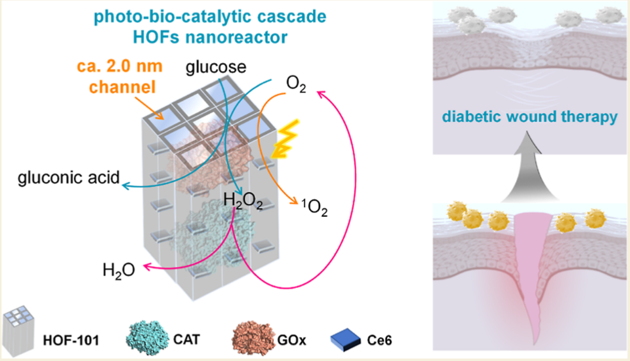

ABSTRACT: A diabetic wound causes thousands of infections or deaths around the world each year, and its healing remains a critical challenge because of the ease of multidrug-resistant (MDR) bacterial infection, as well as the intrinsic hyperglycemic and hypoxia microenvironment that inhibits the therapeutic efficiency. Herein, we pioneer the design of a photobiocatalytic cascade nanoreactor via spatially organizing the biocatalysts and photocatalysts utilizing a hydrogen-bonded organic framework (HOF) scaffold for diabetic wound therapy. The HOF scaffold enables it to disperse and stabilize the host cargos, and the formed long-range-ordered mesochannels also facilitate the mass transfer that enhances the cascade activity. This integrated HOF nanoreactor allows the continuous conversion of overexpressed glucose and H_2O_2 into toxic reactive oxygen species by the photobiocatalytic cascade. As a result, it readily reverses the microenvironment of the diabetes wound and exhibits an extraordinary capacity for wound healing through synergistic photodynamic therapy. This work describes the first example of constructing an all-in-one HOF bioreactor for antimicrobial diabetes wound treatment and showcases the promise of combined biocatalysis and photocatalysis achieved by using an HOF scaffold in biomedicine applications.

KEYWORDS: *hydrogen organic-bonded framework, photobiocatalytic cascade, enzyme immobilization, diabetic wound therapy, nanoreactor*

■ INTRODUCTION

Chronic nonhealing wounds caused by bacterial infection have severely threatened the public's safety and ecological environment for a long time,[1,2] especially susceptible to multidrug-resistant bacteria (MDR)-infected diabetic wounds. The MDR-infected diabetic wounds usually result in serious chronic skin wounds and have resulted in significant morbidity and mortality worldwide. Traditional antibiotics, as the most efficient microbial infection strategy, were once all the rage in the past few decades. Unfortunately, the worldwide overuse of continuous generation of antibiotics in healthcare has exaggeratively pushed them to the limits, triggering the evolution of microorganisms into drug-resistant strains and even the constant emergence of MDR "superbacteria."[3,4]

Antimicrobial photodynamic therapy (aPDT), a noninvasive and unconventional treatment, features the virtues of limited drug resistance, minimal invasiveness, great selectivity, and no side effects, which has been recognized as a promising technique for various bacteria-infected disease wound therapies. It relies on the photoinduced generation of cytotoxic reactive oxygen species (ROS), especially singlet oxygen ($^1O_2$), which eagerly binds with polysaccharides, lipids, and proteins to destroy bacterial membranes and organelles and ultimately results in cell death.[5,6] Nevertheless, the aPDT efficiency is still restricted in the MDR-infected diabetic wound healing because (1) most photosensitizers have limited clinical applications attributable to their defects such as easy aggregation, poor water solubility, and less accumulation on the bacterial surface,[7,8] (2) in addition to high H_2O_2-expressive inflammation,[9] the hostile hyperglycemic environment in diabetic wounds can cause the constriction of blood vessels and inhibit angiogenesis, and hence prolong the scarring or nonhealable wounds that impede the healing process,[10,11] (3) aPDT relies on a successive oxygen consumption process, which hugely exacerbates local hypoxia in the original hypoxic microenviron-

Received: May 25, 2022
Revised: August 10, 2022
Accepted: August 10, 2022
Published: August 19, 2022

https://doi.org/10.1021/jacsau.2c00321

Scheme 1. Schematic Representation of the Photobiocatalytic Cascade HOF Nanoreactor for Accelerating Diabetic Wound Healing

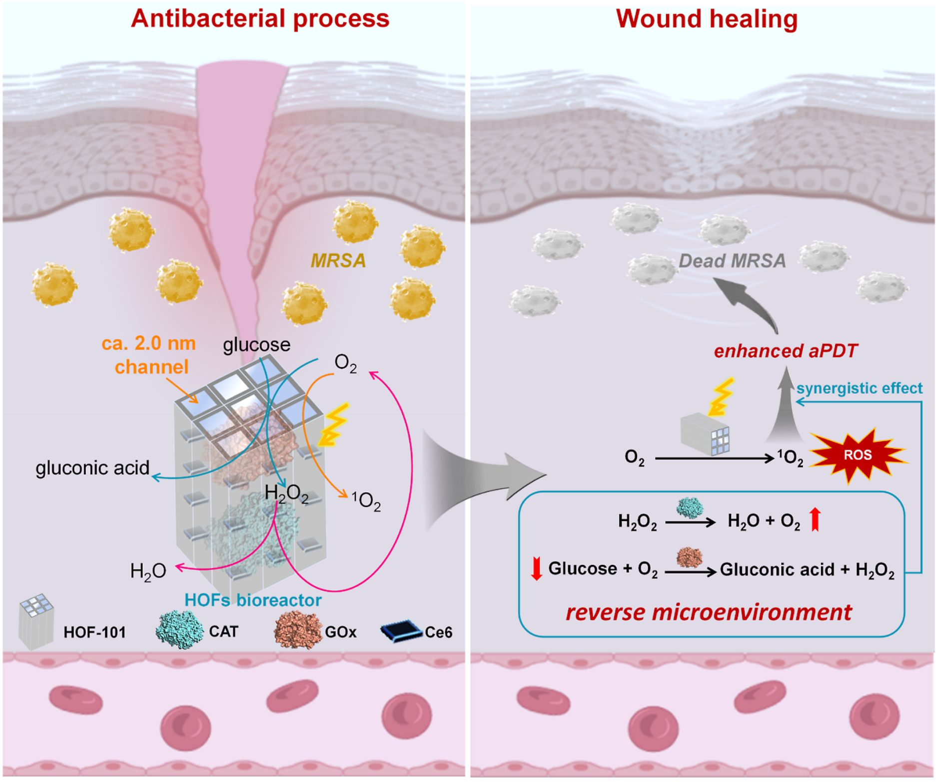

ment to largely constrict the aPDT therapeutic outcomes.[12] Besides, MDR-infected diabetic wound healing is a complicated process including three phases: inflammation, proliferation, and tissue remodeling.[13] Therein, the hypoxic environment is aggravated by the aggregation of highly oxygen-consuming inflammatory cells, but the prolonged oxygen deprivation in chronic trauma severely delays wound healing. Hitherto, massive efforts have been invested in exploiting oxygen-generating systems.[14,15] It is urgently needed to conceive new aPDT strategies circumventing the aforementioned challenges for MDR-infected diabetic wounds therapy.

Rational encapsulation of biofunctional proteins into porous organic frameworks, mainly focused on metal−organic frameworks (MOFs), is advanced nanotechnology for restoring the enzymatic function in a cell-free environment,[16−19] which provides new insights into the next-generation nanobiosystem for different applications. However, the most widely used MOF matrix, zeolitic imidazolate framework-8 (ZIF-8), has a narrowly crystallographic aperture (ca. 3.4 Å) that restrains the mass transfer for biocatalysis and also limits the subsequent loading of therapeutic cargos.[20] As a class of emerging porous crystal materials, hydrogen-bonded organic frameworks (HOFs) hold a reticular chemistry with high porosity, large specific surface areas, and tailored pore size/shape.[21,22] Beyond that, hydrogen-bonded linkage topology endows HOFs with several distinct merits such as mild synthetic condition, easy recyclability, and excellent biocompatibility benefiting from their metal-free attribute. Such structural features provide new opportunities for designing the alternative HOF bionanosystem, yet the proof-of-concept biomedical study is scarce because the HOF chemistry is still in its infancy, most likely due to its low structural stability of hydrogen-bonded linkage.[23−25]

Herein, we integrated a photobiocatalytic cascade HOF nanoreactor that enabled the continuous toxic ROS generation, as well as glucose- and H_2O_2-activated oxygen pumping, for antimicrobial diabetes wound therapy. The inspiration for this HOF bioreactor was drawn from the natural biocascade,[26] which enabled the intracellular biotransformation of unwanted substances into on-demand biomolecule utilizing tandem enzymatic reactions. The photocatalyst and cascading enzymes, involving glucose oxidase (GOx) and catalase (CAT), were spatially immobilized within a mesoporous HOFs scaffold. The HOF skeleton dispersed and stabilized the host cargos, and its mesoporous channel ensured the high accessibility of the internalized biocatalysts that favored the biomimetic cascade process (Scheme 1). By means of the photobiocatalytic cascade of our HOF bioreactors, the excessive endogenous glucose and H_2O_2 in diabetes wound could efficiently convert into highly active singlet oxygen *in situ*. This process relieved the hyperglycemic and hypoxic microenvironment and accelerated the aPDT process for diabetic wound healing.

RESULTS AND DISCUSSION

Design and Characterization of the Photobiocatalytic Cascade HOF

HOF-101, also termed as PFC-1,[27,28] was selected as the framework for engineering the photobiocatalytic cascade nanoreactor because (1) HOF-101 is topologically constructed by a large π-conjugated photosensitizer, termed as 1,3,6,8-tetrakis(*p*-benzoic acid)pyrene (H_4TBAPy). Such reticular linkage allows the spatial organization of H_4TBAPy and enlarges the π-conjugated system, and these features advance

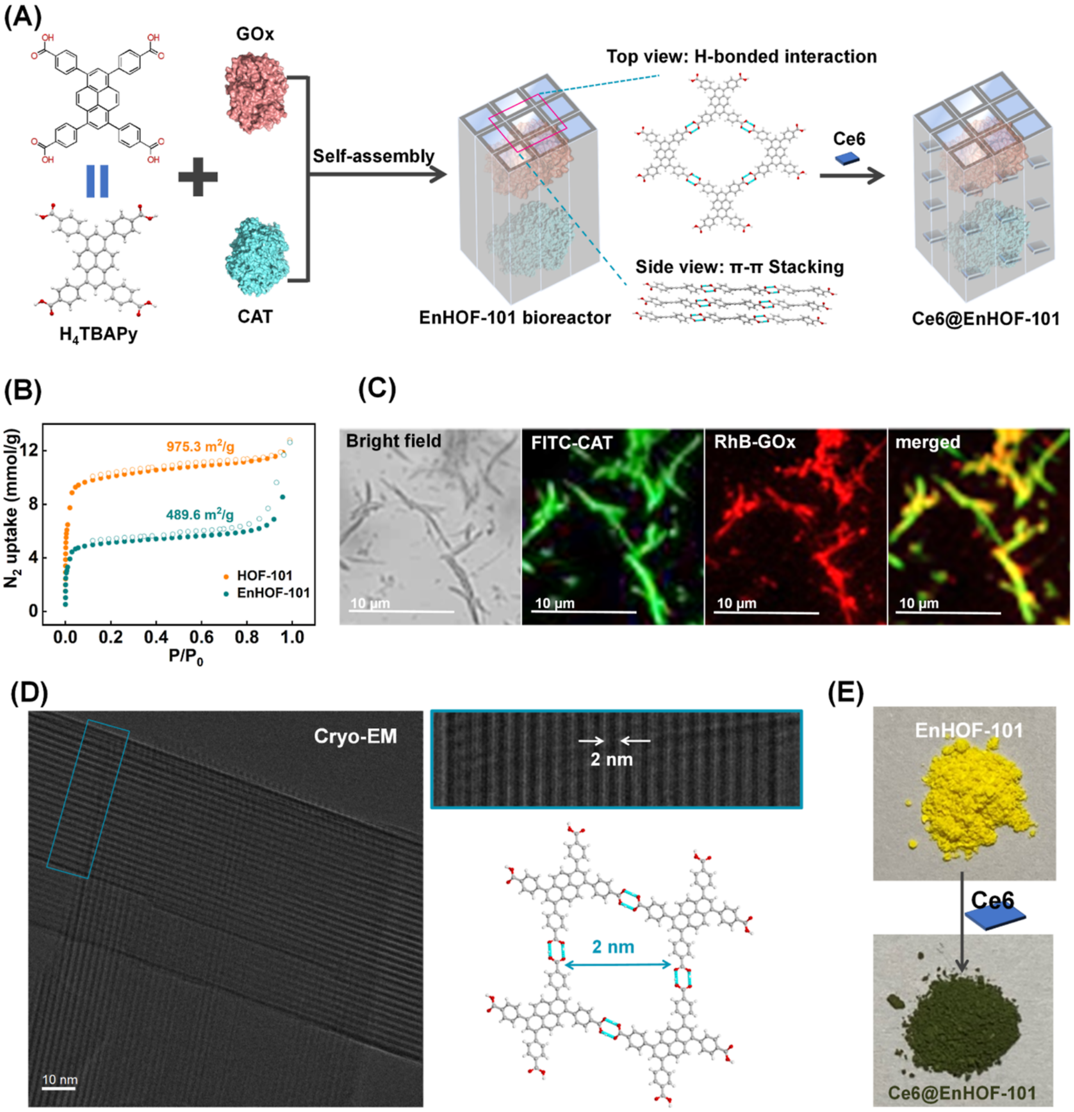

Figure 1. (A) Schematic representation of the preparation of the photobiocatalytic cascade HOF-101 nanoreactor. (B) N_2 adsorption/desorption isotherms of HOF-101 before and after enzyme encapsulation. (C) CLSM images of the spatial distribution of CAT and GOx within HOF-101. Note that the HOF-101 has weak green fluorescence, which has been deducted in the CLSM imaging of FITC-CAT. (D) Cryo-EM image of the designed HOF-101 nanoreactor. (E) Digital photographs of the EnHOF-101 before and after Ce6 loading.

the photodynamic efficiency; (2) the layer-by-layer $\pi-\pi$ stacking affords HOF-101 high chemical stability in a wide range of pH (pH = 1−12).[27,28] Considering the mild crystallization process of HOFs and the large molecular size of enzymes (CAT: 4.9 × 4.4 × 5.6 nm; GOx: 6.0 × 5.2 × 7.7 nm, Figure S1), the bulky biocargos, including GOx and CAT, were spatially confined within the HOF-101 scaffold via an *in situ* approach[24] (Figure 1A, the biocomposite was denoted as EnHOF-101), followed by loading the photosensitizer, chlorin e6 (Ce6), within the topological mesopores to reinforce the photodynamic capacity (Figure 1A, the bioreactor was denoted as Ce6@EnHOF-101).

The powder X-ray diffraction patterns of the synthesized EnHOF-101 and Ce6@EnHOF-101 well inherited the Bragg diffraction peaks of the parent HOF-101 (Figure S2), indicating that the crystallinity was reserved. The scanning electron microscopy (SEM) image presented a rod-like nanostructure of the as-synthesized Ce6@EnHOF-101 (Figure S3A), which was in agreement with that of HOF-101 (Figure S3B). To examine the encapsulation of enzymes, we first designed an adsorption experiment (details seen in the supplementary methods section in the Supporting Information and Figure S4), which elucidated that the bulky GOx and CAT (GOx: 6.0 × 5.2 × 7.7 nm; CAT: 4.9 × 4.4 × 5.6 nm, Figure S1) were impossible to be surface-adsorbed onto or post-infiltrate into the as-synthesized HOF-101. In the Fourier-transform infrared spectra (Figure S5), the spectral bands at 1700−1610 cm^{-1} and 1595−1480 cm^{-1} in EnHOF-101 were designated as the amide I band and amide II band of the peptide skeleton of the enzymes,[29] attesting the successful incorporation of enzymes. Besides, the loading of the enzymes was further supported by the nitrogen adsorption/desorption isotherm experiments (Figure 1B). The nitrogen−adsorption amount of EnHOF-101 [calculated Brunner−Emmet−Teller (BET) surface area: 489.6 m^2/g] was significantly reduced in comparison to that of the pure HOF-101 (calculated BET surface area: 975.3 m^2/g). Also, the calculated pore volume of EnHOF-101 dynamically decreased at the same time (Figure S6), indicating the successful loading of enzymes. A closer examination of the spatial distribution of enzymes in EnHOF-

https://doi.org/10.1021/jacsau.2c00321
JACS Au 2022, 2, 2048−2058

101 was carried out by confocal laser scanning microscopy (CLSM) experiment, where the CAT and GOx were prelabelled with the green dye fluorescein isothiocyanate (FITC) and the red dye rhodamine B (RhB), respectively. As displayed in Figure 1C, the overlapped fluorescence elucidated that both GOx and CAT were confined throughout the HOF-101 scaffold. Furthermore, the enzyme-loading efficiencies, calculated according to fluorescence intensity changes (Figure S7) in the supernatants before and after encapsulation, were ca. 18.3 and 15.8 wt % for CAT and GOx, respectively (Table S1). These results together demonstrated that both CAT and GOx were efficiently encapsulated into HOF-101.

To clarify if the enzymes could reserve their original activity after encapsulation, we also synthesized the GOx-encapsulated HOF-101 (GHOF-101) and CAT-encapsulated HOF-101 (CHOF-101), respectively, using a similar *in situ* approach (Figure S8). The catalytic rates (Figure S9) of GHOF-101 and CHOF-101 were slightly inferior to the free GOx and CAT at the same enzyme dosage (Figure S10). These slight decreases in activities after encapsulation were caused by the inevasible inhibition of the substrate diffusion process by the host shell.[30−32] It was worth noting that compared with the free enzyme, much higher activity conversions were observed in EnHOF-101 after exposure to different nonphysiological conditions, including high temperature (60 °C), polar solvent (acetone), proteolytic enzyme (5 mg/mL trypsin), and denatured reagent (6 M urea), respectively (Figure S11). Such enhancement in stability was attributed to the robust and porous HOF-101 shell shielding the enzyme against denaturation. These experimental results together verified that the enzymes involving GOx and CAT were successfully encapsulated into HOF-101 while maintaining desirable bioactivities.

We next attempted to unveil the microstructure of EnHOF-101 using low-electron-dose cryoelectron microscopy (Cryo-EM, Figure 1D). With Cryo-EM, the lattice planes along the (0 1 1) direction and its well-organized 1D channel-like mesopores (ca. 2.0 nm) could be clearly witnessed throughout the framework. This crystallographic structure was in line with the standard HOF-101, suggesting that the biocargo encapsulation could not change the topological linkage, in which the intrinsic 1D channel-like mesopores were well reserved. Such a long-order mesoporous channel favors the loading of small reagents, such as Ce6 photosensitizer (ca. 16.1 × 14.0 Å, Figure S12). After Ce6 loading, the obtained Ce6@EnHOF-101 showed an apparent color change (Figure 1E), indicating the successful immobilization of Ce6, which was also supported by another CLSM imaging experiment (Figure S13). The UV−vis spectra analysis gave a loading of Ce6 as high as 23.9 wt % (Figure S14 and Table S3). In addition, we found that the UV−vis absorption band of Ce6 was slightly redshifted in Ce6@HOF-101, indicating the host−guest interaction between Ce6 and HOF-101 scaffold (Figure S15).

In order to improve the dispersibility and biocompatibility of the prepared Ce6@HOF-101, a hydrophilic and biocompatible polymer, polyvinylpyrrolidone (PVP), was modified onto its surface. As presented in Figure S16, after PVP surface modification, Ce6@EnHOF-101 showed a significantly reduced water contact angle from 134.97 to 60.85°, suggesting an enhancement in hydrophilicity. In addition, the successful surface modification of PVP was also confirmed by the zeta (ζ) potential experiment (Figure S17). As a result, Ce6@EnHOF-101 after PVP modification displayed higher dispersibility compared to the raw Ce6@EnHOF-101, as evidenced by the dynamic light scattering analyses (Figure S19A). Moreover, the PVP-modified Ce6@EnHOF-101 retained good dispersion even after placing at room temperature for 24 h (Figure S18B).

Biocatalytic Cascade Activity

We began to evaluate the biocatalytic cascade performance of the designed Ce6@EnHOF-101. Notably, we beforehand optimized the ratio of GOx to CAT during the preparation of Ce6@EnHOF-101 and selected the best Ce6@EnHOF-101 in terms of the glucose consumption capacity (the GOx: CAT ratio (w/w) of 1:1 was the optimized value, Figure S19). This optimized Ce6@EnHOF-101 was used for the following experiments. Viewing the microenvironment of the MDR-infected diabetic wound shows that it has high concentrations of glucose and H_2O_2 that inhibit wound healing. Thus, controlling and reversing this adverse microenvironment is of vital importance. In the biocascade process of GOx-CAT enzymes (Figure 2A), the glucose could be oxidized and converted into gluconic acid and H_2O_2 by GOx with the participation of O_2 (eq 1), and the endogenous or newly generated H_2O_2 could be decomposed into O_2 by CAT (eq 2). In this sense, this cascade reaction permitted the continued scavenging of glucose and H_2O_2, yet the supplement of substantial O_2, enabling to relieve the hyperglycemic and hypoxic microenvironment. At the same time, the continuous supplement of O_2 also facilitated the generation of toxic ROS ($^1O_2$) under the aPDT process (eq 3), which should expedite the killing of MDR bacteria.

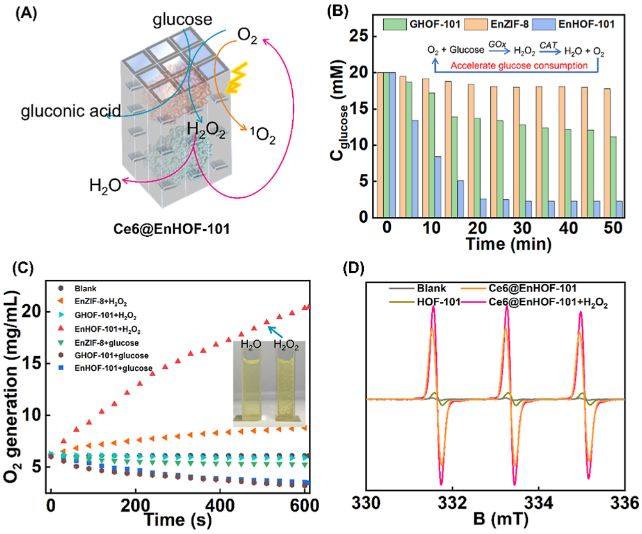

Figure 2. (A) Photobiocatalytic cascade in Ce6@EnHOF-101 nanoreactors. Time-dependent glucose consumption (B) and O_2 generation (C). Concentrations of all nanoparticles remained the same (1 mg/mL) in (B,C). (D) Identified $^1O_2$ by EPR using TEMP as the probe. The concentrations of all nanoparticles remained the same (1 mg/mL), and all of the trials were irradiated with 45 mW/cm^2 of white light for 10 min before the EPR measurement.

$$\text{glucose} + O_2 \xrightarrow{\text{GOx}} \text{gluconic acid} + H_2O_2 \tag{1}$$

$$H_2O_2 \xrightarrow{\text{CAT}} H_2O + O_2 \tag{2}$$

$$O_2 \xrightarrow{\text{Ce6@EnHOF} - 101,\ h\nu} {}^1O_2 \tag{3}$$

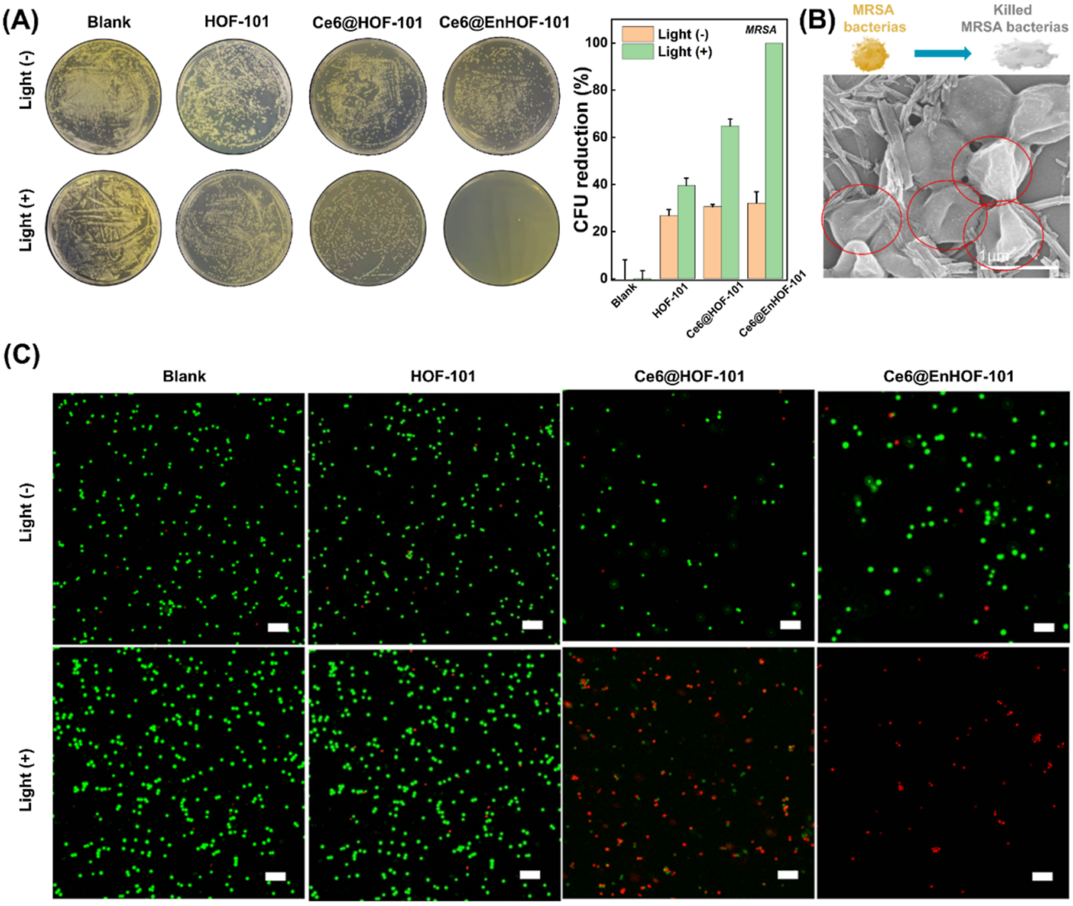

Figure 3. (A) Photographs of the MRSA bacterial colonies after treatments with different materials (left) and the corresponding bacterial viability (right). All the experimental groups that required irradiation were irradiated with 45 mW/cm^2 of white light for 10 min, and all groups were then incubated in an incubator at 37 °C overnight before the evaluation. (B) Collapse and shrinkage morphology of MRSA after treatment with Ce6@EnHOF-101 under white light irradiation for 10 min. (C) SYTO9/PI two-color fluorescent images for the live (green fluorescence) and dead (red fluorescence) bacterial staining assay of MRSA. Scale bar: 5 μm.

As illustrated in Figure 2B, when Ce6@EnHOF-101 was incubated with 20 mM glucose solution, the glucose could be continuously consumed, accompanied by the pH decreasing because of the generation of gluconic acid (Figure S20A). In addition, the efficiency of glucose decomposition was much superior to the counterpart without CAT loading in the same GOx dosage (the GHOF-101 group in Figure 2B), verifying that the regeneration of O_2 by CAT, in turn, improved the glucose decomposition. At the same time, the O_2 concentration was observed to be slightly decreased under the catalytic process of GOx (Figure 2C). Such a slightly decreased O_2 concentration was also observed in the GHOF-101 because of the aerobian biocatalysis of GOx (Figure 2C). However, in the presence of H_2O_2, Ce6@EnHOF-101 could accelerate O_2 generation with the concentration increasing from 6.11 to 20.35 mg/L in 600 s, and abundant O_2 bubbles were clearly observed during this biocatalytic process (the inset in Figure 2C). As a comparison, in the presence of H_2O_2, no produced O_2 was recorded in GHOF-101 on account of the absence of CAT. These results together illustrated that our biocatalytic cascade EnHOF-101 indeed enabled us to decompose glucose and H_2O_2 while producing O_2.

To highlight the advantages of the GOx-CAT biocatalytic cascade, we synthesized the EnHOF-101 analogue through coencapsulation of the cascading enzymes consisting of GOx and peroxidase (horseradish peroxidase, HRP), and this analogue was denoted as GHHOF-101 (Figure S8). The biocascade reaction of GOx-HRP is also able to decompose glucose and H_2O_2, which has been widely explored for nanocatalytic medicine.[33,34] As shown in Figure S21A, our EnHOF-101 outperformed GHHOF-101 with respect to glucose decomposition. This was attributed to the regeneration of O_2 by CAT in the GOx-CAT biocatalytic cascade, in which the regenerated O_2, in turn, improved the efficiency of glucose decomposition (Figure 2B). Moreover, in the presence of H_2O_2, the O_2 production assay displayed in Figure S21B showed that our EnHOF-101 could accelerate O_2 generation, ascribing to the efficient breakdown of H_2O_2 by CAT. However, GHHOF-101 was unable to generate O_2 because the peroxidase activity of HRP was unable to convert H_2O_2 into O_2. Therefore, the presented GOx-CAT biocatalytic cascade showcased enhanced activity in terms of glucose and H_2O_2 consumption, as well as O_2 generation.

The channel-like mesopores of HOF-101 should enhance the accessibility of the encapsulated enzymes and might favor the biocatalytic cascade. To verify this conjecture, the micropore ZIF-8 was also selected as the scaffold to construct a similar biocatalytic cascade nanoreactor because the mild crystallization condition of ZIF-8 allows it to encapsulate many enzymes via an *in situ* approach[16−19,30,31,35−39] (details seen in the Supporting Information, Figures S22−S24). The biocascade activity of our Ce6@EnHOF-101, in terms of glucose decomposition (Figures 2B and S20B) and H_2O_2-activated O_2 generation capacity (Figure 2C), significantly outperforms the Ce6@EnZIF-8 counterpart at the same enzymes dosage and testing conditions. Such enhancement in the biocascade ability was attributed to the different crystallographic structures (Figure S25). HOF-101 has a much larger crystallographic pore (24.5 × 18.6 Å) compared to ZIF-8 (3.4 Å).[40] On the basis of the biocascade activity, we speculated that the channel-like mesopores of HOF-101 accelerated the diffusion of the catalytic substrate that favored the biocatalysis, but this mechanism required further experiments to confirm.

The antibacterial efficacy of the aPDT process depends greatly on ROS production. Therefore, we first investigated the photoinduced ROS production of our Ce6@EnHOF-101 nanoreactor using 2,7-dichlorofluorescein diacetate (DCFH-DA) as the ROS probe, wherein nonfluorescent DCFH-DA could be oxidized to highly fluorescent 2,7-dichlorofluorescein in the presence of ROS.[41] We noted that our Ce6@EnHOF-101 possessed higher ROS production than the Ce6@EnZIF-8 counterpart (Figure S26) under the same nanomaterial amounts. This resulted from the larger pore of HOF-101, facilitating Ce6 loading (Table S3, 23.9 wt % in Ce6@EnHOF-101, while 4.3 wt % in Ce6@EnZIF-8), and the incorporation of Ce6 indeed could strengthen the ROS generation of HOF-101 (Figure S27).

A closer examination of the ROS species was carried out by electron paramagnetic resonance (EPR) spectra, in which the dominated ROS was identified as $^1O_2$ using 2,2,6,6-tetramethylpiperidine as the probe (Figure 2D). HOF-101 is periodically linked by a large π-conjugated photosensitizer of H_4TBAPy. It endowed HOF-101 with an inherent capacity for phototriggered $^1O_2$ generation, which was much superior to the free H_4TBAPy molecule (Figure S28). After loading the Ce6 into the mesopore of En@HOF-101, the ability of $^1O_2$ generation of the formed Ce6@EnHOF-101 was dramatically improved (Figure 2D). Importantly, in the existence of H_2O_2, the EPR signal of the generated $^1O_2$ was further enhanced. This was attributed to the continuous supply of O_2 through H_2O_2 decomposition by CAT (Figure 2C), in turn, facilitating the conversion of O_2 to $^1O_2$ under light irradiation. In addition, the positive effect of CAT on $^1O_2$ generation was also supported by another control experiment, wherein EnHOF-101 outperformed GHOF-101 (without CAT) in terms of $^1O_2$ generation under an equal H_2O_2 concentration (Figure S29).

Antibacterial Performance against Multiple-Resistant *Staphylococcus aureus*

A diabetic wound has a typically hyperglycemic microenvironment compared to conventional wounds. Encouraged by the high biocascade activity and $^1O_2$ generation capacity of the designed photobiocatalytic cascade HOF nanoreactor, the antibacterial performance against multiple-resistant *staphylococcus aureus* (MRSA) under the simulated hyperglycemia environment was investigated by a classical plate count method. All the experimental groups requiring irradiation were irradiated with 45 mW/cm^2 of white light for 10 min and then incubated in an incubator at 37 °C overnight. As shown in Figure 3A, the antibacterial activities were comprehensively assessed by various treatment groups: (1) blank, (2) HOF-101, (3) Ce6@HOF-101, (4) Ce6@EnHOF-101, (5) blank + light, (6) HOF-101 + light, (7) Ce6@HOF-101 + light, and (8) Ce6@EnHOF-101 + light. Without the light irradiation, the number of bacterial colonies in group (2) to (4) was less than 32% colony-forming units (CFU), implying that the MRSA killing was limited without $^1O_2$ generation (Figure 3A). Whereas under the light irradiation for 10 min, both Ce6@HOF-101 and Ce6@EnHOF-101 showed dynamically improved abilities for killing MRSA bacteria, which were much superior to the pure HOF-101. This was ascribed to the high loading and well-dispersive Ce6 in the mesopore of HOF-101, which significantly enhanced the toxic $^1O_2$ production. Extraordinarily, Ce6@EnHOF-101 presented extremely efficient antibacterial ability with an inhibition rate up to near 100% (CFU = 99.9%, Figure 3A), while ca. 35% MRSA bacteria still survived using Ce6@HOF-101 (CFU = 64.9%, Figure 3A). Besides, a further insight into the time-dependent bacterial growth also confirmed the superior antibacterial performance of Ce6@EnHOF-101 (Figure S30). Such extraordinary antimicrobial ability of Ce6@EnHOF-101 verified the important role of the microenvironment modulation by biocascade cascade. That is, based on the designed biocascade reaction, Ce6@EnHOF-101 could continuously catalyze glucose into oxygen, as evidenced by the decreasing glucose concentration around the bacterial colony (Figure S31). This glucose consumption could cut off the nutrients for bacterial growth, which efficiently inhibited bacterial proliferation. In addition, the cell exposure experiment also confirmed that our Ce6@EnHOF-101 indeed could promote the O_2 generation under the simulated hyperglycemic and H_2O_2-overexpressed microenvironment (Figure S32), and the newly produced O_2 advanced the highly toxic $^1O_2$ conversion under an aPDT process.

To further illustrate the advantages of our HOF system on antibacterial performance, the in vitro antibacterial experiment using the Ce6@EnZIF-8 analogue was also carried out (Figure S33). Under similar light irradiation, the designed Ce6@EnHOF-101 displayed remarkable enhancement in the antibacterial ability compared with Ce6@EnZIF-8. This was comprehensible because the channel-like mesoporous HOF-101 scaffold favored the biocascade efficiency and the phototriggered $^1O_2$ generation, which were well demonstrated in Figures 2 and S26.

To closely understand the antibacterial mechanism, the morphology changes in MRSA were first unveiled in various treatment groups. No obvious morphology changes were found in the SEM images of group (1) to (6), in which the typical spherical shape of MRSA with membrane integrity, a clear boundary, and a smooth surface remained (Figure S34). As a comparison, in group (7), Ce6@HOF-101 resulted in the partial collapse and shrinkage in the cell membrane of MRSA (Figure S34). It should be noted that using our Ce6@EnHOF-101 nanoreactors in group (8), the bacterial membranes were seriously damaged by cell wall fragmentation and completely lost their primary spherical morphologies (Figure 3B). In order to revalidate the antibacterial mechanism, the two-color live/dead cell analysis by fluorescent imaging was conducted (Figure 3C), where SYTO9 and propidium iodide (PI) were applied to differentiate the living bacteria (green fluorescence) and dead bacteria (red fluorescence), respectively. As expected, the bright green fluorescence was observed in group (1) to (6), indicating that the vast majority of *MRSA* was still alive. By contrast, a mass of dead bacteria was identified in group (7). More importantly, almost all bacteria were killed using our Ce6@EnHOF-101 nanoreactors in group (8). These results together demonstrated that the photobiocatalytic cascade HOF nanoreactors could effectively relieve the hyperglycemic

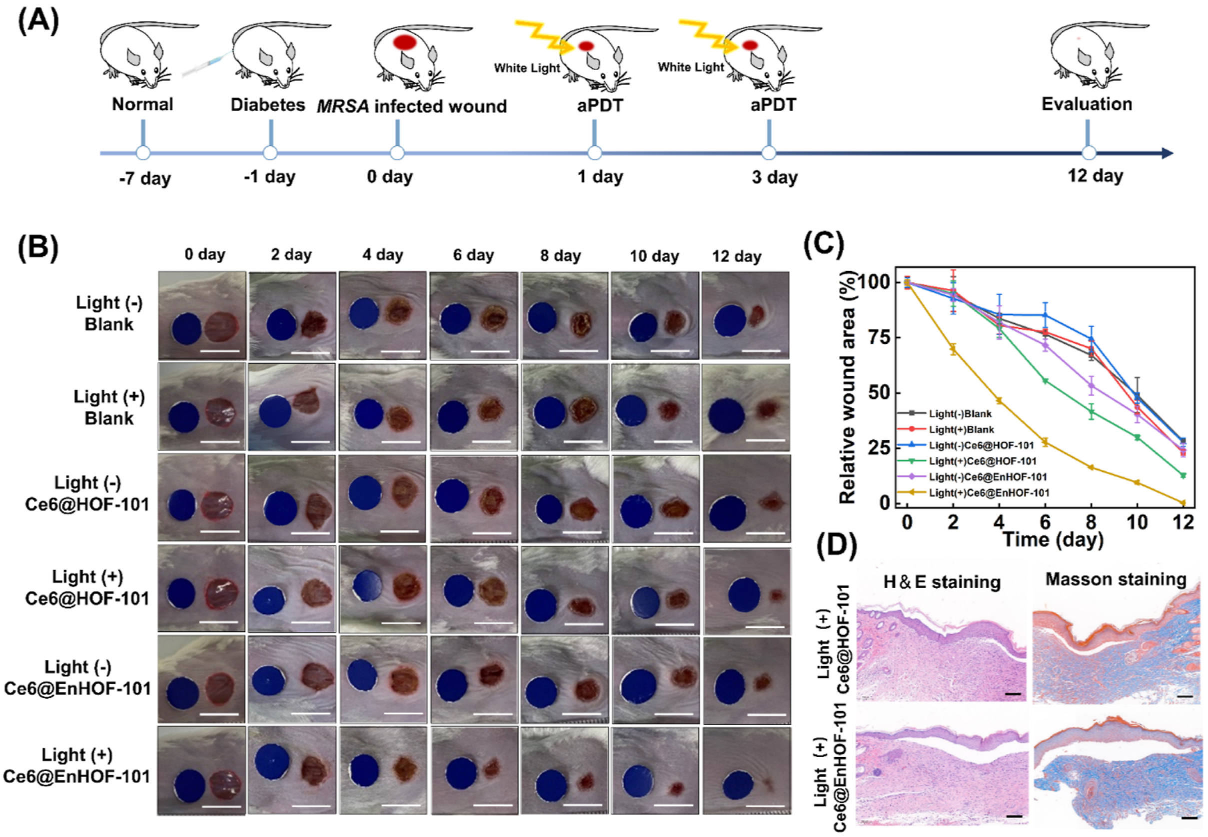

Figure 4. (A) Schematic diagram of the construction of the MRSA-infected diabetic model and the treatment strategy. (B) Photographs of the MRSA-infected diabetic mice wounds in different groups. Each wound was administered every 2 d, and the blank group was treated with PBS. Scale bar: 1 cm. (C) Time-dependent changes in wound areas. (D) H&E and Masson staining images of wound tissue slices after treatment for 12 days. Scale bar: 100 μm.

and hypoxic microenvironment and exhibited extraordinary antimicrobial ability through a synergistic photodynamic therapy.

In Vivo Diabetic Wound Therapy

The *in vivo* antibacterial activity was evaluated on a bacteria-infected diabetic mice model, in which circular wounds with a diameter of 0.8 cm were inflicted on the back of the mice and then infected with MRSA (50 μL, OD_{600} = 1.0) for 24 h (Figure 4A). The MRSA-infected mice were randomly assigned into six groups (n = 5 for each group) based on the different treatments: (1) blank, (2) blank + light, (3) Ce6@HOF-101, (4) Ce6@HOF-101 + light, (5) Ce6@EnHOF-101, and (6) Ce6@EnHOF-101 + light. The dosages of the materials were kept at 100 μg/mL. At day 1 and 3, the mice were anesthetized with isoflurane gas, and 40 μL of materials solution (100 μg/mL) was dropped onto the wound and irradiated with white light (45 mW/cm^2) for 30 min. In order to observe the wound healing situation, the wounds were photographed at day 0, 2, 4, 6, 8, 10, and 12. As seen from the wound healing processes in Figure 4B, without the light irradiation in groups (3) and (5), both Ce6@HOF-101 and Ce6@EnHOF-101 could not advance the wound healing compared to the blank group (1), which was caused by the limited antibacterial abilities in dark conditions (Figure 3A). However, under the light irradiation, our Ce6@EnHOF-101 nanoreactor dynamically accelerated wound healing, significantly outperforming the Ce6@HOF-101 counterpart. Notably, on the fourth day, the wound area treated by Ce6@EnHOF-101 became visually smaller. After treatment over 8 days, an obviously scabbed wound was noticed, and the wound was almost healed in 12 days, manifesting the highly efficient diabetic wound therapy through the synergistic effect of the photobiocatalytic cascade in our Ce6@EnHOF-101 nanoreactor. Such a synergistic effect on wound therapy was also elucidated by the time-dependent changes in the wound area (Figure 4C), wherein the rate of wound area reduction in the Ce6@EnHOF-101 group was much faster than other groups including Ce6@HOF-101. Furthermore, hematoxylin and eosin (H&E) (Figure S35) and Masson (Figure S36) staining were applied to evaluate the wound healing statuses. As shown in Figure 4D, the Ce6@EnHOF-101-treated wound exhibited no obvious inflammation in H&E staining and maximum collagen fibers in Masson staining, demonstrating that the proposed Ce6@EnHOF-101 nanoreactor could effectively promote the healing of infected diabetes wounds.

We next investigated the biocompatibility of Ce6@EnHOF-101. Initially, the hemolysis assay was conducted under different Ce6@EnHOF-101 concentrations. Figure S37 showed that no obvious hemolysis was observed by coculturing Ce6@EnHOF-101 with red blood cells (RBCs). Then, the thiazolyl tetrazolium (MTT) assay (Figure S38) was carried out on 293T normal cells to assess the cytotoxicity of Ce6@EnHOF-101, in which no observable toxicity was found. Afterward, the toxicity assay of major organs and blood tests were carried out. There were no significant lesions or inflammation in the major organs, such as the heart, liver, spleen, lung, and kidney (Figure S39). The routine blood test showed that the RBC, white blood cell, hemoglobin, hematocrit, mean corpuscular volume, mean corpuscular hemoglobin (MCH), MCH concentration (MCHC), and platelets (PLT) levels of mice in various treatment groups presented similar results (Figure S40). Further examination by blood biochemical analyses revealed that there were no distinct differences in the contents of albumin, alanine aminotransferase, aspartate aminotransferase, creatinine, lactate dehydrogenase, total protein, uric acid, and urea among the various test groups (Figure S41). These results together demonstrated the good biocompatibility of our Ce6@EnHOF-101 nanoreactor, ascribing to the metal-free attribute of HOF and the mild conditions required in both photocatalysis and biocatalysis.

■ CONCLUSIONS

In summary, we engineered a biomimetic cascade nanoreactor through spatially organizing enzymes and photosensitizers into a mesoporous HOF scaffold. It allowed the *in situ* conversion of overexpressed glucose and H_2O_2 into useful O_2 in the diabetes wound, which effectively relieved the hyperglycemic and hypoxic microenvironment through the biocatalytic cascade. In addition, the substantial O_2 production further boosted the highly toxic $^1O_2$ generation and thus advanced the synergetic aPDT-based diabetic wound therapy. In comparison to the microporous ZIF-8 counterpart, our photobiocatalytic cascade HOFs exhibited enhanced biocascade activity and ROS generation capacity on account of the larger pore channel that favored the confined biocatalysis, as well as the Ce6 cargo loading. It resulted in a much higher antibacterial performance of our HOF nano-biosystem compared to the well-known ZIF-8 counterpart. Considering the metal-free feature and the biocompatible assembling condition of HOFs, we believe that our work may provide new insights into the design and synthesis of biosafe HOF nanobiosystem for a broad range of biomedical applications.

■ METHODS

Synthesis of the Ce6@EnHOF-101 Photobiocatalytic Cascade Nanoreactor

Ce6@EnHOF-101 was prepared through a mild *de novo* assembly method, with some modifications.[24] 10 mg of H_4TBAPy was dissolved into 1 mL of DMF through ultrasonic treatment. Then, 9 mL of pH 4 enzyme aqueous solution (containing 2.5 mg GOx and 2.5 mg CAT) was quickly poured into the H_4TBAPy solution under stirring at room temperature in the dark. After 5 min stirring, the mixed solution was aged for another 15 min, and the EnHOF-101 hybrid was formed. Subsequently, 400 μL of Ce6 (10 mg/mL in DMF) was introduced, and the Ce6 permeated into the channel-like mesopore of EnHOF-101 under stirring for 10 min.

After centrifugation, the obtained Ce6@EnHOF-101 precipitate was dispersed in 5 mL of PVP aqueous solution (4 mg/mL) and stirred at room temperature for 2 h in the dark. Finally, the prepared Ce6@EnHOF-101 was collected by centrifugation and washed with deionized water two times and ethanol one time. In the case of activity tests and therapeutic applications, the collected Ce6@EnHOF-101 was directly washed with deionized water three times and stored at 4 °C.

Enzyme Loading Measurement

The multienzyme loadings in EnHOF-101 and EnZIF-8 were evaluated by the fluorescence labeling experiments. To quantify each enzyme, GOx was labeled with RhB (a red dye), while CAT was labeled with FITC (a green dye). In the assembly process, the raw enzymes were replaced by the dye-labeled enzymes, and other steps were similar to the aforementioned descriptions.

The loading of each enzyme was measured by examining the corresponding fluorescence decrease in the supernatant before and after encapsulation via fluorescence spectra. The FITC-CAT and RhB-GOx were quantified at λ_{em} = 520 nm (488 nm excitation) and λ_{em} = 583 nm (540 nm excitation), respectively.

Antibacterial Experiments

For simulating the microenvironment of a diabetes wound, the antibacterial experiments were carried out in a hyperglycemia condition, and they were divided into eight groups (n = 3 in each group): (1) PBS, (2) HOF-101, (3) Ce6@HOF-101, (4) Ce6@EnHOF-101, (5) PBS + light, (6) HOF-101 + light, (7) Ce6@HOF-101 + light, and (8) Ce6@EnHOF-101 + light. The concentrations of different nanoparticles, sterile PBS, and glucose used in the experiments were 500 μg/mL, 10, and 20 mM, respectively. First, MRSA solutions (OD_{600} = 1.0) were mixed with the sample solutions of group (1) to (8), respectively, and incubated for 30 min at 37 °C. Then, group (5) to (8) were subjected to white light irradiation (45 mW/cm^2) for 10 min, while group (1) to (4) were kept in the dark for 10 min. Then, the pathogen suspension was diluted 5×10^2 folds with sterile PBS, and 100 μL of diluted pathogen suspension was spread onto a solid agar plate. Finally, all of the agar plates were incubated in an incubator at 37 °C overnight. The number of CFUs was recorded to evaluate the antibacterial performance. The inhibition ratio (IR) was calculated based on the following equation (eq 4)

$$\mathrm{IR} = \frac{C_0 - C}{C_0} \times 100\% \tag{4}$$

where C is the CFU of the experimental group treated with the sample solution, and C_0 is the CFU of the control group without any treatment.

Antibacterial Performance *in Vivo*

All experiments on mice in our research were carried out following the approved protocol by Institutional Animal Care and Use Committee of the Shenzhen People's hospital (AUP-220402-YHT-0189-01), and the experiments were conducted in accordance with relevant institutional and national guidelines and regulations.

To evaluate the *in vivo* antibacterial property of Ce6@EnHOF-101, the wound model was built on the back of the diabetic mice. The BALB/C mice (male, 6−8 weeks) were purchased from Gem Pharma Tech, China, and were maintained under specific pathogen-free conditions in the animal center of the Shenzhen People's hospital. The diabetes mice models were established by injecting streptozotocin (STZ, Gentihold Biotechnology Co., Ltd., Beijing, China) through intraperitoneal injection. The blood glucose level was measured after 7 d. When the blood glucose level was above 16.7 mM, the model was considered successful. After anaesthetization, the hair on the skin was shaved off, and the surface was sterilized with 70% alcohol prior to the creation of wounds. A wound with a diameter of 0.8 cm on mice was made, and the MRSA suspension (1.0×10^8 CFU, 50 μL) was subsequently injected into the wound. The infected wound model was built after 24 h bacteria reproduction.

Then, the mice were divided into six groups (n = 5 for each group) for different treatments: (1) blank, (2) blank + light, (3) Ce6@HOF-101, (4) Ce6@HOF-101 + light, (5) Ce6@EnHOF-101, and (6) Ce6@EnHOF-101 + light. The dosages of the materials used were kept at 100 μg/mL. On day 1 and 3, the mice were anesthetized with isoflurane gas, and 40 μL of materials solution (100 μg/mL) was dropped onto the wound and irradiated with white light (45 mW/cm^2) for 30 min. In order to observe the wound healing situation, the wounds were photographed on day 0, 2, 4, 6, 8, 10, and 12. On day 12, all mice were sacrificed, and the skin tissue around the wounds was carefully collected and fixed with 4% paraformaldehyde solution to prepare the pathological slides. Finally, the tissue sections were stained by H&E and Masson staining. Meanwhile, the blood of the animals was obtained by the infraorbital plexus blood collection method for further analysis.

Other Methods

Other methods are provided in the supplementary method section in the Supporting Information.

ASSOCIATED CONTENT

Supporting Information

The Supporting Information is available free of charge at https://pubs.acs.org/doi/10.1021/jacsau.2c00321.

Experimental method, characterization data of materials, and biological experimental data (PDF)

AUTHOR INFORMATION

Corresponding Authors

Jigang Wang − *Department of Geriatric Medicine, Shenzhen People's Hospital, The Second Clinical Medical College, Jinan University, Shenzhen 518020, China*; Email: jgwang@icmm.ac.cn

Siming Huang − *Guangzhou Municipal and Guangdong Provincial Key Laboratory of Molecular Target and Clinical Pharmacology, the NMPA and State Key Laboratory of Respiratory Disease, School of Pharmaceutical Sciences and the Fifth Affiliated Hospital, Guangzhou Medical University, Guangzhou 511436, China*; orcid.org/0000-0002-0912-1082; Email: huangsm@gzhmu.edu.cn

Guosheng Chen − *MOE Key Laboratory of Bioinorganic and Synthetic Chemistry, School of Chemistry, Sun Yat-sen University, Guangzhou 510275, China*; orcid.org/0000-0002-6540-7675; Email: chengsh39@mail.sysu.edu.cn

Authors

Wei Huang − *School of Chemical Engineering and Technology, Sun Yat-sen University, Zhuhai 519082, China*

Haitao Yuan − *Department of Geriatric Medicine, Shenzhen People's Hospital, The Second Clinical Medical College, Jinan University, Shenzhen 518020, China*; orcid.org/0000-0001-6141-7254

Huangsheng Yang − *MOE Key Laboratory of Bioinorganic and Synthetic Chemistry, School of Chemistry, Sun Yat-sen University, Guangzhou 510275, China*

Linjing Tong − *MOE Key Laboratory of Bioinorganic and Synthetic Chemistry, School of Chemistry, Sun Yat-sen University, Guangzhou 510275, China*

Rui Gao − *MOE Key Laboratory of Bioinorganic and Synthetic Chemistry, School of Chemistry, Sun Yat-sen University, Guangzhou 510275, China*

Xiaoxue Kou − *MOE Key Laboratory of Bioinorganic and Synthetic Chemistry, School of Chemistry, Sun Yat-sen University, Guangzhou 510275, China*

Xiaomin Ma − *Cryo-EM Center, Southern University of Science and Technology, Shenzhen 518055, China*

Fang Zhu − *MOE Key Laboratory of Bioinorganic and Synthetic Chemistry, School of Chemistry, Sun Yat-sen University, Guangzhou 510275, China*; orcid.org/0000-0002-6939-9975

Gangfeng Ouyang − *School of Chemical Engineering and Technology, Sun Yat-sen University, Zhuhai 519082, China; MOE Key Laboratory of Bioinorganic and Synthetic Chemistry, School of Chemistry, Sun Yat-sen University, Guangzhou 510275, China*; orcid.org/0000-0002-0797-6036

Complete contact information is available at: https://pubs.acs.org/10.1021/jacsau.2c00321

Author Contributions

□W.H. and H.Y. contributed equally. CRediT: **Huangsheng Yang** methodology, software; **Gangfeng Ouyang** funding acquisition, resources, supervision, writing-review & editing.

Author Contributions

W.H. and H.Y. contributed equally to this work. G.C. conceived the idea and designed the experiments. W.H. and H.Y. carried out the experiments and analyzed the data. H.Y., L.T., R.G., X.K., and F.Z. participated in the discussion. X.M. helped with the Cryo-EM imaging. G.C., S.H., J.W., and G.O. supervised the experiments and provided financial support. G.C., S.H., and W.H. co-wrote the manuscript. CRediT: **Wei Huang** investigation, methodology, visualization, writing-original draft; **Haitao Yuan** investigation, methodology, validation, visualization; **Huangsheng Yang** methodology, software; **Linjing Tong** software; **Rui Gao** software; **Xiaoxue Kou** software; **Jigang Wang** formal analysis, funding acquisition, resources, validation; **Xiaomin Ma** methodology, resources; **Siming Huang** formal analysis, funding acquisition, supervision, writing-review & editing; **Fang Zhu** resources; **Guosheng Chen** conceptualization, data curation, formal analysis, funding acquisition, project administration, resources, supervision, writing-original draft, writing-review & editing; **Gangfeng Ouyang** funding acquisition, resources, supervision, writing-review & editing.

Notes

The authors declare no competing financial interest.

ACKNOWLEDGMENTS

The authors acknowledge the financial support from projects of the National Natural Science Foundation of China (22174164, 22104159, and 21904146) and the Natural Science Foundation of Guangdong Province (2020A1515010824, 2019A1515011722).

REFERENCES

(1) Falanga, V. Wound Healing and Its Impairment in the Diabetic Foot. *The Lancet* **2005**, *366*, 1736−1743.

(2) Wu, H.; Li, F.; Shao, W.; Gao, J.; Ling, D. Promoting Angiogenesis in Oxidative Diabetic Wound Microenvironment Using a Nanozyme-Reinforced Self-Protecting Hydrogel. *ACS Cent. Sci.* **2019**, *5*, 477−485.

(3) Van Boeckel, P.; Pires, J.; Silvester, R.; Zhao, C.; Song, J.; Criscuolo, G.; Gilbert, M.; Bonhoeffer, S.; Laxminarayan, R. Global trends in antimicrobial resistance in animals in low- and middle-income countries. *Science* **2019**, *365*, No. eaaw1944.

(4) Reverter, M.; Sarter, S.; Caruso, D.; Avarre, J.-C.; Combe, M.; Pepey, E.; Pouyaud, L.; Vega-Heredía, S.; de Verdal, H.; Gozlan, R. E. Aquaculture at the Crossroads of Global Warming and Antimicrobial Resistance. *Nat. Commun.* **2020**, *11*, 1870.

(5) Galstyan, A.; Schiller, R.; Dobrindt, U. Boronic Acid Functionalized Photosensitizers: A Strategy to Target the Surface of Bacteria and Implement Active Agents in Polymer Coatings. *Angew. Chem., Int. Ed.* **2017**, *56*, 10362−10366.

(6) Karges, J. Clinical Development of Metal Complexes as Photosensitizers for Photodynamic Therapy of Cancer. *Angew. Chem., Int. Ed.* **2022**, *61*, No. e202112236.

(7) Hu, D.; Sheng, Z.; Gao, G.; Siu, F.; Liu, C.; Wan, Q.; Gong, P.; Zheng, H.; Ma, Y.; Cai, L. Activatable Albumin-Photosensitizer Nanoassemblies for Triple-modal Imaging and Thermal-Modulated Photodynamic Therapy of Cancer. *Biomaterials* **2016**, *93*, 10−19.

(8) Park, J.; Jiang, Q.; Feng, D.; Mao, L.; Zhou, H.-C. Size-Controlled Synthesis of Porphyrinic Metal-Organic Framework and Functionalization for Targeted Photodynamic Therapy. *J. Am. Chem. Soc.* **2016**, *138*, 3518−3525.

(9) Eming, A.; Martin, P.; Tomic-Canic, M. Wound Repair and Regeneration: Mechanisms, Signaling, and Translation. *Sci. Transl. Med.* **2014**, *6*, 265sr6.

(10) Zhu, Y.; Zhang, J.; Song, J.; Yang, J.; Du, Z.; Zhao, W.; Guo, H.; Wen, C.; Li, Q.; Sui, X.; Zhang, L. A Multifunctional Pro-Healing Zwitterionic Hydrogel for Simultaneous Optical Monitoring of pH and Glucose in Diabetic Wound Treatment. *Adv. Funct. Mater.* **2020**, *30*, 1905493.

(11) Wimmer, R. A.; Leopoldi, A.; Aichinger, M.; Wick, N.; Hantusch, B.; Novatchkova, M.; Taubenschmid, J.; Hämmerle, M.; Esk, C.; Bagley, J. A.; Lindenhofer, D.; Chen, G.; Boehm, M.; Agu, C. A.; Yang, F.; Fu, B.; Zuber, J.; Knoblich, J. A.; Kerjaschki, D.; Penninger, J. M. Human Blood Vessel Organoids as a Model of Diabetic Vasculopathy. *Nature* **2019**, *565*, 505−510.

(12) Sun, X.; Sun, J.; Sun, Y.; Li, C.; Fang, J.; Zhang, T.; Wan, Y.; Xu, L.; Zhou, Y.; Wang, L.; Dong, B. Oxygen Self-Sufficient Nanoplatform for Enhanced and Selective Antibacterial Photodynamic Therapy against Anaerobe-Induced Periodontal Disease. *Adv. Funct. Mater.* **2021**, *31*, 2101040.

(13) Guan, Y.; Niu, H.; Liu, Z.; Dang, Y.; Shen, J.; Zayed, M.; Ma, L.; Guan, J. Sustained Oxygenation Accelerates Diabetic Wound Healing by Promoting Epithelialization and Angiogenesis and Decreasing Inflammation. *Sci. Adv.* **2021**, *7*, No. eabj0153.

(14) Pan, X.; Wang, W.; Huang, Z.; Liu, S.; Guo, J.; Zhang, F.; Yuan, H.; Li, X.; Liu, F.; Liu, H. MOF-Derived Double-Layer Hollow Nanoparticles with Oxygen Generation Ability for Multimodal Imaging-Guided Sonodynamic Therapy. *Angew. Chem., Int. Ed.* **2020**, *59*, 13557−13561.

(15) Jia, Q.; Ge, J.; Liu, W.; Zheng, X.; Chen, S.; Wen, Y.; Zhang, H.; Wang, P. A Magnetofluorescent Carbon Dot Assembly as an Acidic H 2 O 2 -Driven Oxygenerator to Regulate Tumor Hypoxia for Simultaneous Bimodal Imaging and Enhanced Photodynamic Therapy. *Adv. Mater.* **2018**, *30*, 1706090.

(16) Chen, W.-H.; Vázquez-González, M.; Zoabi, A.; Abu-Reziq, R.; Willner, I. Biocatalytic Cascades Driven by Enzymes Encapsulated in Metal-Organic Framework Nanoparticles. *Nat. Catal.* **2018**, *1*, 689−695.

(17) Liang, W.; Xu, H.; Carraro, F.; Maddigan, N. K.; Li, Q.; Bell, S. G.; Huang, D. M.; Tarzia, A.; Solomon, M. B.; Amenitsch, H.; Vaccari, L.; Sumby, C. J.; Falcaro, P.; Doonan, C. J. Enhanced Activity of Enzymes Encapsulated in Hydrophilic Metal-Organic Frameworks. *J. Am. Chem. Soc.* **2019**, *141*, 2348−2355.

(18) Hu, C.; Bai, Y.; Hou, M.; Wang, Y.; Wang, L.; Cao, X.; Chan, C.-W.; Sun, H.; Li, W.; Ge, J.; Ren, K. Defect-Induced Activity Enhancement of Enzyme-Encapsulated Metal-Organic Frameworks Revealed in Microfluidic Gradient Mixing Synthesis. *Sci. Adv.* **2020**, *6*, No. eaax5785.

(19) Tong, L.; Huang, S.; Shen, Y.; Liu, S.; Ma, X.; Zhu, F.; Chen, G.; Ouyang, G. Atomically Unveiling the Structure-Activity Relationship of Biomacromolecule-Metal-Organic Frameworks Symbiotic Crystal. *Nat. Commun.* **2022**, *13*, 951.

(20) Liang, W.; Wied, P.; Carraro, F.; Sumby, C. J.; Nidetzky, B.; Tsung, C.-K.; Falcaro, P.; Doonan, C. J. Metal-Organic Framework-Based Enzyme Biocomposites. *Chem. Rev.* **2021**, *121*, 1077−1129.

(21) Russell, A.; Evans, C.; Li, W.; Ward, D. Nanoporous Molecular Sandwiches: Pillared Two-Dimensional Hydrogen-Bonded Networks with Adjustable Porosity. *Science* **1997**, *276*, 575−579.

(22) Lin, R.-B.; He, Y.; Li, P.; Wang, H.; Zhou, W.; Chen, B. Multifunctional Porous Hydrogen-bonded Organic Framework Materials. *Chem. Soc. Rev.* **2019**, *48*, 1362−1389.

(23) Liang, W.; Carraro, F.; Solomon, M. B.; Bell, S. G.; Amenitsch, H.; Sumby, C. J.; White, N. G.; Falcaro, P.; Doonan, C. J. Enzyme Encapsulation in a Porous Hydrogen-Bonded Organic Framework. *J. Am. Chem. Soc.* **2019**, *141*, 14298−14305.

(24) Chen, G.; Huang, S.; Shen, Y.; Kou, X.; Ma, X.; Huang, S.; Tong, Q.; Ma, K.; Chen, W.; Wang, P.; Shen, J.; Zhu, F.; Ouyang, G. Protein-Directed, Hydrogen-Bonded Biohybrid Framework. *Chem* **2021**, *7*, 2722−2742.

(25) Tang, Z.; Li, X.; Tong, L.; Yang, H.; Wu, J.; Zhang, X.; Song, T.; Huang, S.; Zhu, F.; Chen, G.; Ouyang, G. A Biocatalytic Cascade in an Ultrastable Mesoporous Hydrogen-Bonded Organic Framework for Point-of-Care Biosensing. *Angew. Chem., Int. Ed.* **2021**, *60*, 23608−23613.

(26) Good, C.; Zalatan, G.; Lim, A. Scaffold Proteins: Hubs for Controlling the Flow of Cellular Information. *Science* **2011**, *332*, 680−686.

(27) Ma, K.; Li, P.; Xin, J. H.; Chen, Y.; Chen, Z.; Goswami, S.; Liu, X.; Kato, S.; Chen, H.; Zhang, X.; Bai, J.; Wasson, M. C.; Maldonado, R. R.; Snurr, R. Q.; Farha, O. K. Ultrastable Mesoporous Hydrogen-Bonded Organic Framework-Based Fiber Composites toward Mustard Gas Detoxification. *Cell Rep. Phys. Sci.* **2020**, *1*, 100024.

(28) Yin, Q.; Zhao, P.; Sa, R.-J.; Chen, G.-C.; Lü, J.; Liu, T.-F.; Cao, R. An Ultra-Robust and Crystalline Redeemable Hydrogen-Bonded Organic Framework for Synergistic Chemo-Photodynamic Therapy. *Angew. Chem., Int. Ed.* **2018**, *57*, 7691−7696.

(29) Jackson, M.; Mantsch, H. H. The Use and Misuse of FTIR Spectroscopy in the Determination of Protein Structure. *Crit. Rev. Biochem. Mol. Biol.* **1995**, *30*, 95−120.

(30) Liao, F.-S.; Lo, W.-S.; Hsu, Y.-S.; Wu, C.-C.; Wang, S.-C.; Shieh, F.-K.; Morabito, J. V.; Chou, L.-Y.; Wu, K. C. W.; Tsung, C.-K. Shielding against Unfolding by Embedding Enzymes in Metal-Organic Frameworks via a de Novo Approach. *J. Am. Chem. Soc.* **2017**, *139*, 6530−6533.

(31) Wu, X.; Yue, H.; Zhang, Y.; Gao, X.; Li, X.; Wang, L.; Cao, Y.; Hou, M.; An, H.; Zhang, L.; Li, S.; Ma, J.; Lin, H.; Fu, Y.; Gu, H.; Lou, W.; Wei, W.; Zare, R. N.; Ge, J. Packaging and Delivering Enzymes by Amorphous Metal-Organic Frameworks. *Nat. Commun.* **2019**, *10*, 5165.

(32) Chen, S.-Y.; Lo, W.-S.; Huang, Y.-D.; Si, X.; Liao, F.-S.; Lin, S.-W.; Williams, B. P.; Sun, T.-Q.; Lin, H.-W.; An, Y.; Sun, T.; Ma, Y.; Yang, H.-C.; Chou, L.-Y.; Shieh, F.-K.; Tsung, C.-K. Probing Interactions between Metal-Organic Frameworks and Freestanding Enzymes in a Hollow Structure. *Nano Lett.* **2020**, *20*, 6630−6635.

(33) Kumar, S.; Karmacharya, M.; Michael, I. J.; Choi, Y.; Kim, J.; Kim, I.; Cho, Y.-K. Programmed Exosome Fusion for Energy Generation in Living cells. *Nat. Catal.* **2021**, *4*, 763−774.

(34) Zhang, Y.; Tsitkov, S.; Hess, H. Proximity Does not Contribute to Activity Enhancement in the Glucose Oxidase-Horseradish Peroxidase Cascade. *Nat. Commun.* **2016**, *7*, 13982.

(35) Liang, K.; Ricco, R.; Doherty, C. M.; Styles, M. J.; Bell, S.; Kirby, N.; Mudie, S.; Haylock, D.; Hill, A. J.; Doonan, C. J.; Falcaro, P. Biomimetic Mineralization of Metal-Organic Frameworks as Protective Coatings for Biomacromolecules. *Nat. Commun.* **2015**, *6*, 7240.

(36) Lyu, F.; Zhang, Y.; Zare, R. N.; Ge, J.; Liu, Z. One-Pot Synthesis of Protein-Embedded Metal-Organic Frameworks with Enhanced Biological Activities. *Nano Lett.* **2014**, *14*, 5761−5765.

(37) Chen, G.; Huang, S.; Kou, X.; Wei, S.; Huang, S.; Jiang, S.; Shen, J.; Zhu, F.; Ouyang, G. A Convenient and Versatile Amino-Acid-Boosted Biomimetic Strategy for the Nondestructive Encapsulation of Biomacromolecules within Metal-Organic Frameworks. *Angew. Chem., Int. Ed.* **2019**, *58*, 1463−1467.

(38) Chen, G.; Huang, S.; Kou, X.; Zhu, F.; Ouyang, G. Embedding Functional Biomacromolecules within Peptide-Directed Metal-Organic Framework (MOF) Nanoarchitectures Enables Activity Enhancement. *Angew. Chem., Int. Ed.* **2020**, *59*, 13947−13954.

(39) Chen, G.; Kou, X.; Huang, S.; Tong, L.; Shen, Y.; Zhu, W.; Zhu, F.; Ouyang, G. Modulating the Biofunctionality of Metal-Organic-Framework-Encapsulated Enzymes through Controllable Embedding Patterns. *Angew. Chem., Int. Ed.* **2020**, *59*, 2867−2874.

(40) Park, S. K.; Ni, Z.; Côté, P.; Choi, Y.; Huang, R.; Uribe-Romo, J.; Chae, K.; O'Keeffe, M.; Yaghi, M. Exceptional Chemical and

Thermal Stability of Zeolitic Imidazolate Frameworks. *Proc. Natl. Acad. Sci. U.S.A.* **2006**, *103*, 10186−10191.

(41) Bourré, L.; Thibaut, S.; Briffaud, A.; Rousset, N.; Eléouet, S.; Lajat, Y.; Patrice, T. Indirect Detection of Photosensitizer Ex Vivo. *J. Photochem. Photobiol., B* **2002**, *67*, 23−31.